



Fabrication and characterization of differentiated aramid nanofibers and transparent films

Jingjing Luo¹ · Meiyun Zhang^{1,2,4} · Bin Yang^{1,3,4} · Guodong Liu¹ · Shunxi Song¹

Received: 7 December 2017 / Accepted: 13 March 2018 / Published online: 26 March 2018
© Springer-Verlag GmbH Germany, part of Springer Nature 2018

Abstract

Aramid nanofibers (ANFs) frequently are employed as versatile building blocks for constructing high-performance nanocomposites due to its structural and performance superiority. In this paper, the different ANFs and ANF films derived from the typical aramid yarns, chopped fiber, pulp fiber and fibril fiber, respectively, were fabricated through deprotonation with potassium hydroxide in dimethyl sulphoxide, protonation with deionized water and vacuum-assisted filtration. The physical tests such as tensile test, ultraviolet transmittance and absorbance, thermogravimetric analysis were executed to evaluate and contrast the thermodynamic and optical performances of these differentiated ANFs and ANF films. The analytical results suggested that ANFs films prepared by the different forms of aramid macrofibers presented with differentiated properties such as mechanical behaviors, transparencies and flexibilities. And also it was found that the oversized nanofiber in length led to the formation of flocculation which was adverse for ANFs films in the formation of high strength. Whereas, small diameter just facilitated for the achievement of high stiffness and transparency. By contrast, the ANFs films made from chopped nanofiber, with aspect ratio of 200–500, exhibited good transparency, thermal stability and mechanical properties with transmittance value of 83%, TG10% around 521 °C, ultimate strength (σ) of 103.41 MPa, stiffness (E) of 4.70 GPa and strain at break of 5.56%. This work offers an alternative nanoscale building block as an effective nanofiller for preparing high-performance nanocomposites with different requirements in the potential fields such as transparent coating and flexible electrode or display materials, battery separator and microporous membrane.

Keywords Aramid nanofibers fabrication · Deprotonation · Transparent film · Characterization

✉ Meiyun Zhang
myzhang@sust.edu.cn

✉ Bin Yang
lxyangbin@126.com

¹ Shaanxi Provincial Key Laboratory of Papermaking Technology and Specialty Paper Development, National Demonstration Center for Experimental Light Chemistry Engineering Education, College of Bioresources Chemical and Materials Engineering, Shaanxi University of Science and Technology, Xi'an 710021, People's Republic of China

² State Key Laboratory for Modification of Chemical Fibers and Polymers Materials, Donghua University, Shanghai 201620, People's Republic of China

³ School of Science, Key Laboratory of Space Applied Physics and Chemistry of Ministry of Education, Northwestern Polytechnical University, Xi'an 710072, People's Republic of China

⁴ Present Address: College of Bioresources Chemical and Materials Engineering, National Key Research and Development Program, Shaanxi University of Science and Technology, Xi'an 710021, People's Republic of China

Introduction

High performance fiber, such as aromatic polyamide fiber, has drawn considerable concern in the area of building lightweight and high-strength materials, whose strength is generally greater than 17.6 cN/dtex and elastic modulus should also be above 440 cN/dtex (Grujicic et al. 2013; Nilakantan et al. 2015). Aromatic polyamide fiber, commonly known as aramid fiber, is divided into two basic types, namely poly-paraphenylene terephthalamide (PPTA) and poly-*m*-phenyleneisophthalamide (PMIA) in accordance with different chemical structures (Wu et al. 2012). Compared with PMIA, PPTA fiber as a priority has been developed much more rapidly in the past decades to fabricate some functional materials or products in the fields of aerospace, personal protection and automotive friction material on the basis of the superiority of strength performance (Wu et al. 2012; Wright et al. 2015; Kim et al. 2001; Widodo et al. 2012; Mishra et al. 2014; Aranganathan et al. 2016). PPTA fiber

is commonly classified as four basic forms in the practical application, and termed as yarns, chopped, pulp and fibrid fiber, respectively, according to the different manufacturing processes (as shown in Fig. 1).

Aramid yarns generally are prepared by spinning a liquid concentration of sulfuric acid into a highly crystallized fiber (Yang et al. 2015). The special spinning process leads to the fact that yarns microfibrils are easy to be fibrillated due to the high orientation along the fiber axis and relatively poor bonding strength in the transverse direction (Wollbrett-Blitz et al. 2015). Besides, most of studies have shown that aramid yarns are equipped with the structure of ‘skin–core’ like cable (Takayanagi et al. 1982; Wright et al. 2015). Aramid chopped fibers, produced by mechanical cutting of post-treatment (hot drawing, crimping and drying) yarns, retain the most properties of aramid yarns (Schmitt and Ortlepp 2008; Abu Obaid et al. 2011). In addition, pulp fibers, as one of the differentiated fibrillation products of chopped fibers, are acquired by means of mechanical agitation of chopped fibers or the cut-off yarns in water, whose strength and insulation capacity are inherited from the original fiber (Faramarzi and Razzaghi-Kashani 2015; Yang et al. 2016). For fibrid fibers, serving as a neoteric material which has just been reported recently, are generally manufactured by directly adding the PPTA resin into coagulating bath under the centrifugation of high speed (Hendriks et al. 2004; Lu et al. 2016). The special manufacturing process gives the fibrid fibers the totally different fiber morphology and performances such as good adhesion and thermal bonding properties, which have been widely applied in the paper-based functional materials (Ren et al. 2014).

It is well-known that the outstanding rigid structure of PPTA (seen in Fig. 2) is attributed to the unique molecular structure composing of π - π conjugated system, strong hydrogen bonds and dispersive Van der Waals forces, which can generate the excellent properties of high strength, stiffness, thermal stability and certain dielectric property (Barkoula et al. 2008; Grujicic et al. 2013). Although the large variety of multifunctional composites have been developed by combining aramid microfibers with other materials such as epoxy (Park et al. 2003), polypropylene (Kapoor et al. 2016) and carbon nanotubes (O’Connor et al. 2009)

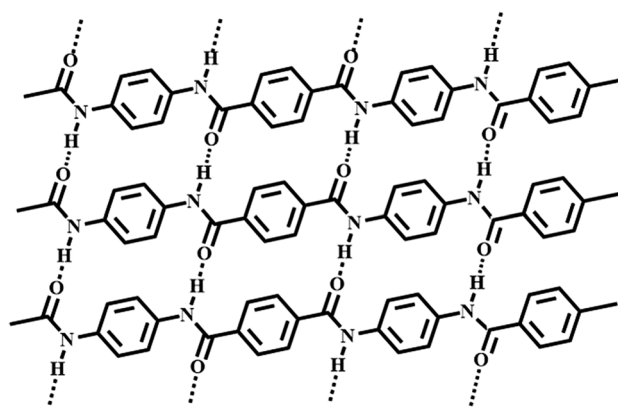
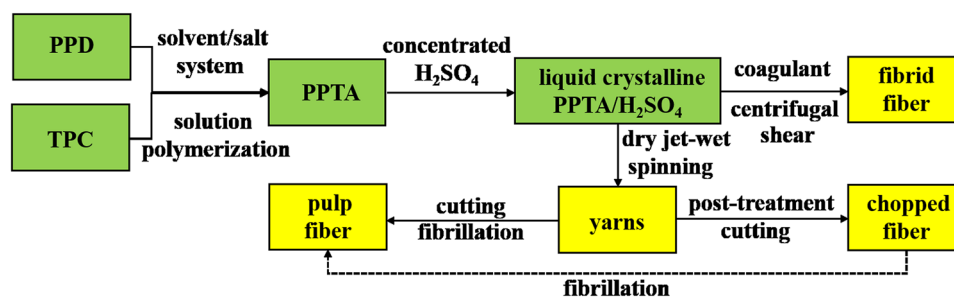


Fig. 2 Imitate intermolecular structure of PPTA

to enhance the strength of the composite materials per se. However, to improve the strength for composite materials in terms of the aramid macrofibers still cannot avoid the potential risk such as poor interfacial strength, which always arises from chemical inertness of the material caused by less exposed active groups of aramid macrofibers (Abdel-Bary et al. 1997; Qin et al. 2017). It indeed has become a critical challenge for the time being and further restricts the application of aramid microfibers to develop novelty functional composite materials.

Nanofiber is frequently employed to improve the poor bonding property of material interface when fabricating the composites (Salehi-Khojin et al. 2007). The major reason for utilizing nanofiber to reinforce interface is due to that much higher surface area is exposed and more active groups generated in nanofiber than the macroscopic fibers, which further increases the interconnectivity possibility of these fibers with external surface. Gardner et al. (2008) proposed that among the structure and properties of nanocellulose such as morphology, crystalline structure, surface properties, the high surface area made adhesion property the most important parameter to control for nanocomposite applications. Recently, Thomas (2017) reported that the nano-enhanced polymer, fabricated by dispersing the graphitized multiwalled carbon nanotubes (MWCNT) into an acrylonitrile butadiene styrene polymer matrix, was successfully

Fig. 1 The schematic diagram of manufacturing processes for the different aramid macrofibers



applied in the full-scale 3D printed components, in which the increased surface area of MWCNT played a prominent part in the design of composites with enhanced mechanical properties. In accordance with application of nanofiber, the study of synthetic aramid nanofiber never started to receive great attention until 2011. Yang et al. (2011) experimentally observed that the aramid nanofibers can be prepared by feasible deprotonation of macroscopic aramid fibers with potassium hydroxide (KOH) in dimethyl sulfoxide (DMSO). And also it was pointed that ANFs obtained as above method have reserved the most physical and chemical properties of the pristine fiber by various characterization. Since then multifarious ANFs-based nanocomposites such as ANFs/Carbon nanotubes (Zhu et al. 2015), ANFs/graphene (Fan et al. 2012; Park et al. 2015), ANFs/epoxy (Lin et al. 2017), ANFs/gold nanoparticles (Lyu et al. 2016b) and ANFs/carbon fibers (Lee et al. 2016) have been keeping reported.

Although all of these reports indicated that ANFs split from macroscale aramid fibers maintain the excellent mechanical properties and have a great capacity to be an innovative strength agent acting as nanoscale building block or nanofiller in preparing high-performance nanocomposites. However, most of the previous studies have just focused the study of Kevlar threads or fabrics of yarns (Li et al. 2016; Nie et al. 2017; Cao et al. 2013), the physical performance differences of the ANFs and ANFs films prepared by these typical macroscale aramid fibers (yarns, chopped, pulp and fibril fibers) have not been explored sufficiently. Inspired the previous work, the different nano-aramid fibers and ANFs

films, therefore, were manufactured from the typical macroscale aramid fibers by means of deprotonation with KOH in DMSO, protonation with deionized water and vacuum-assisted filtration (VAF). The differentiated physical properties (mechanical behaviors, transparencies and flexibilities) of ANFs films were determined by the physical tests such as tensile test, ultraviolet (UV) transmittance and absorbance, thermogravimetric analysis (TGA), et al. The analysis results provide the experimental evidences when using nanoscale aramid fibers to fabricate the composites in practice. The potential applications of ANFs can also be developed in the broad areas of in electrical, transparent coating and filter, et al.

Materials and methods

Preparation of ANFs/DMSO dispersion

The Twaron yarns, chopped, pulp and fibril fibers (seen in Fig. 3a–d) were all obtained from Teijin. Here, the four kinds of fibers were in turn labeled by F1, F2, F3 and F4 whose physical parameters were also listed in Table 1. Dimethyl sulfoxide (DMSO, 99.5%) and anhydrous ethanol (99.7%) were purchased from Tianjin Da Mao Chemical Reagent Co., Ltd. Potassium hydroxide (KOH) and Sodium dodecyl benzene sulfonate (LAS) were provided by Tianjin Ke Meou Chemical Co., Ltd. and Tianli Chemical Reagent Co., Ltd, respectively. All the

Fig. 3 a–d The Photographs of macroscale aramid fibers from F1 to F4; e–h samples of ANFs/DMSO dispersions; i the isolated ANFs powder, j–m samples of ANFs films from F1-ANFs to F4-ANFs

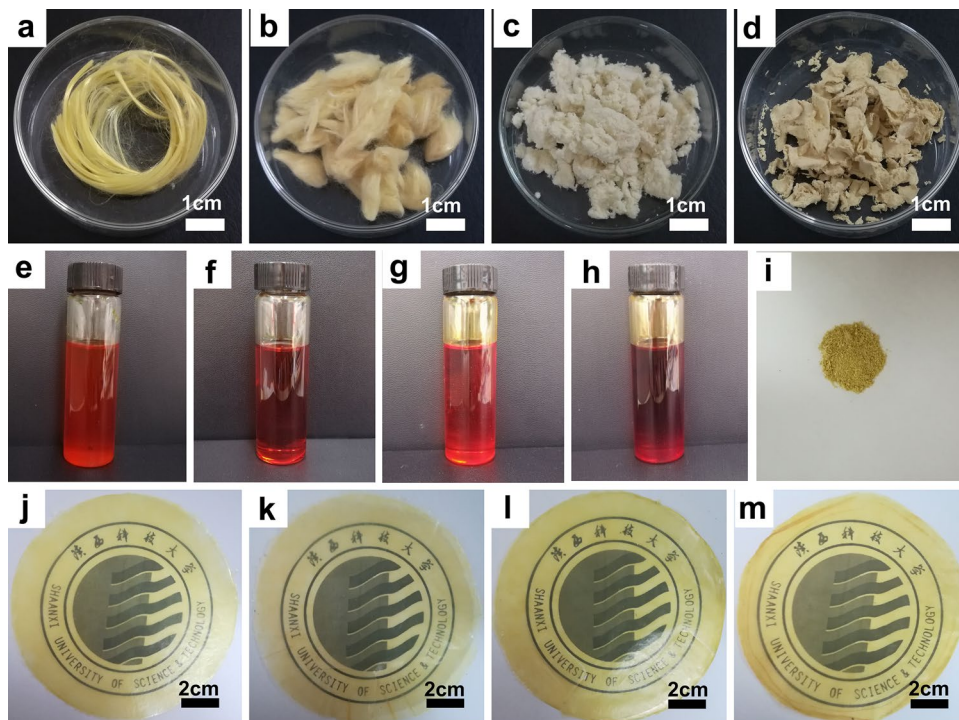


Table 1 For the physical parameters of macroscale aramid fibers

| Fiber | Label name | Length (mm) | Average diameter (μm) | Aspect ratio | Specific surface area (m^2/g) |
|---------|------------|-------------|------------------------------------|--------------|-------------------------------------------------|
| Yarn | F1 | 70–80 | 13.7 | 2900–3700 | 0.59 |
| Chopped | F2 | 4–5 | 12.5 | 300–400 | 0.76 |
| Pulp | F3 | 0.5–2 | 33 | 20–50 | 5.16 |
| Fibrid | F4 | 0.2–1 | 33.7 | 6–30 | 7.43 |

Chemical reagents were directly used. For fibers prior to be used, yarns and chopped fibers were prewashed by LAS to remove the organic residues first and further washed by deionized water to eliminate the bubbles brought by LAS. Pulp and fibrid fibers were directly washed by deionized water.

For the sample preparation, the original aramid fibers, 1.0 g yarns, chopped, pulp and fibrid fibers and 1.5 g KOH, respectively, were added into 500 ml DMSO (Yang et al. 2011). The suspension of experimental sample was then stirred with magnet bar at 550 r/min in a fully enclosed environment for continuous 7 days at ambient lab temperature. Four homogeneous and transparent solutions of ANFs/DMSO (2 mg/mL) were finally obtained, which looked like dark red as seen in Fig. 3e–h.

Isolation of ANFs powder and fabrication of ANFs film

ANFs powder (Fig. 3i) was isolated from the solution by modifying the solubility of nanofibers in DMSO (Lin et al. 2017). Here, two equal volumes of deionized water was added into ANFs/DMSO dispersion first, the continuous magnetic stirring was necessary to generate a uniform ANFs/DMSO/H₂O mixture. Then the solid ANFs were trapped by a nylon filter cloth (500 meshes) under vacuum pressure. Deionized water and acetone were repeatedly used to wash and remove the residual KOH and DMSO remained in ANFs. Finally, the solid ANFs was dried under the ambient atmosphere. For ANFs films, the parallel operations were adopted to form a uniform ANFs/DMSO/H₂O mixture. Followed by ultrasonic dispersion for 10 min to effectively eliminate bubbles existing in the mixture, VAF was employed again to obtain a series of wet ANFs films named by F1-ANFs, F2-ANFs, F3-ANFs and F4-ANFs, which corresponded to the nanoscale aramid fibers from F1 to F4, respectively. With regard to the drying for the samples, ANFs films were first fast dried at 80 °C for 30 min in a circular laboratory sheet former to achieve fast drying and to avoid the formation of wrinkles in the final ANFs films and then dried in oven at 80 °C for another 48 h. The final samples were prepared as shown in Fig. 3j–m.

Characterization

Transmission electron microscopy (TEM) (Tecnai G2 F20 S-TWIN, FEI, US) with a Gatan 832 CCD camera operating at an accelerating voltage of 200 kV was used to observe the morphologies of ANFs in DMSO, which were further evaluated by Scanning-electron microscopy (SEM) (HITACHI-S4800, Rigaku, Japan) under an acceleration voltage of 3.0 kV while the original dry fibers' morphologies and chopped fibers in DMSO/KOH system for different time were obtained using a VEGA3 SBH (TESCAN, Czech) Scanning Electron Microscope at 10 kV accelerating voltage.

Fourier transform infrared (FT-IR) spectra of aramid macrofibers and ANFs films was recorded on a Vertex70 (Bruker, Germany) spectrometer with an attenuated total reflectance (ATR) in a scanning range of 400–4000 cm^{-1} .

X-ray diffraction (XRD) measurements were performed on a D8 Advance (Bruker, Germany) with $\text{CuK}\alpha$ ($\lambda = 0.1542$ nm) generated at 40 kV and 40 mA with the diffraction angle $2\theta = 5\text{--}60^\circ$ and a scanning speed of $6^\circ/\text{min}$ at room temperature.

Thermogravimetric analysis was carried on the Simultaneous TG-DSC thermal analyzer (STA449F3, NETZSCH, Germany) at the heating rate of 10 °C/min in nitrogen gas atmosphere with a certain temperature ranging from 30 to 800 °C.

UV–Vis absorbance and transmittance spectra of the ANFs films were achieved using an UV–visible-near infrared light spectrophotometer (Cary 5000, Agilent Technologies, US).

The thickness of the films was measured by a thickness measuring instrument (DC-HJY03, Sichuan Changjiang, China).

The mechanical properties including stress, strain and elastic modulus of ANFs films were determined using a servo-control tensile testing machine (AI-7000-NGD, Goodtechwill, China) equipped with a 500 kg gravity sensor. Each sample of ANFs film was cut into rectangular strips of 60 mm \times 10 mm and measured with a crosshead speed of 5 mm/min and a gauge length of 30 mm at room temperature, the final mechanical performances of films were confirmed as an average of 5 measurements.

Results and discussion

The physical observation of the raw materials

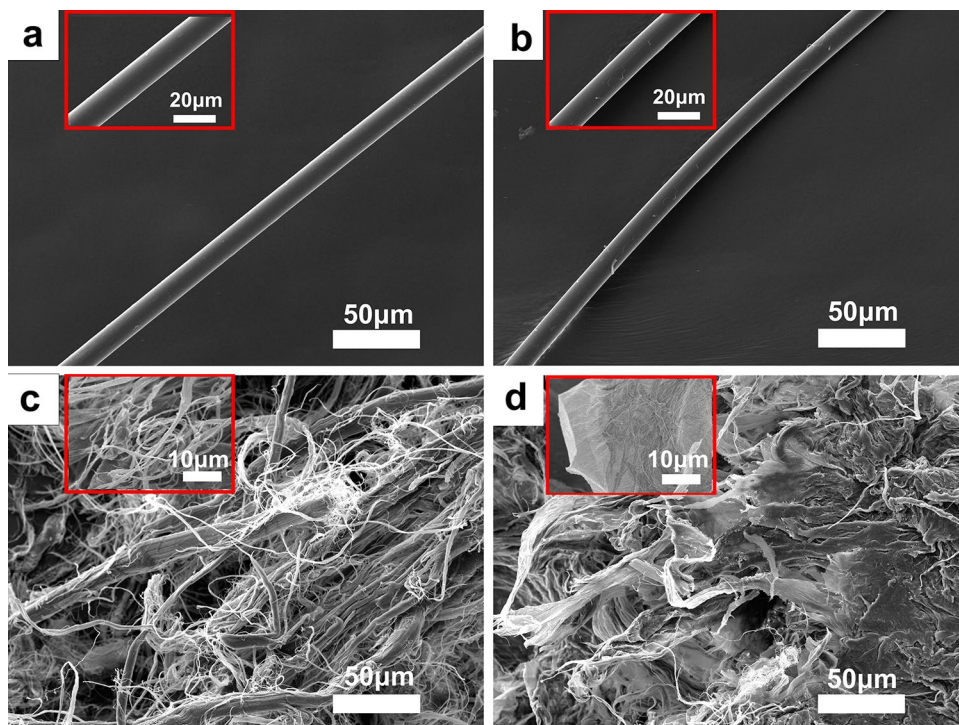
SEM images of the surface structures were used to characterize the different morphologies of the raw materials (Fig. 4). The yarns (Fig. 4a) and chopped fibers (Fig. 4b) presented much more smooth rod-like structure (Lu et al. 2017) as a result of liquid crystal spinning compared with aramid pulp (Fig. 4c) and fibril fibers (Fig. 4d). According to previous reports, the complete ‘skin–core’ structure was kept in both of them (Sa et al. 2014). For pulp fibers (Fig. 4c), rich plush microfibrils were observed obviously, which attributed to the high degree of fibrillation treatment (Faramarzi and Razzaghi-Kashani 2015). Moreover, fibril fibers (Fig. 4d) looked more like the ribbon-shape film with pleated structure because of the special precipitation and coagulation process (Levit and Amma 2006; Kang et al. 2014). Different from the yarns and chopped fibers, the dense ‘skin–core’ structure in pulp and fibril fibers probably was disrupted and higher specific surface area, therefore, was formed as supported in the Table 1 in Sect. 2.1. It was able to be speculated that the morphological differences above can influence the permeation effect and interaction role of DMSO/KOH into the internal structure of PPTA and further prompted some changes in the final ANFs and ANFs films, which was further discussed in the following part.

The mechanism analysis of the formation of ANFs and ANFs films

Four parallel homogeneous and transparent ANFs/DMSO dispersions were fabricated according to the method in Sect. 2.2. For the specific forming mechanism, the chopped fibers (Fig. 5a) as an exemplification was to interpret intrinsic regime of the formation of ANFs and ANFs films as shown in Fig. 5.

The schematic diagram of single aramid chopped fiber in longitudinal, transverse dimension and its intermolecular structure were, respectively, displayed in Fig. 5b–d (the blue dots represent the hidden molecular chain of PPTA), basing on the smooth ‘rod-like’ (Fig. 5d₁) and ‘skin–core’ structure resulting from the special spinning process (Srinivasan and Reneker 1995; Sa et al. 2014; Lu et al. 2017). First, the ‘skin’ layer of macrofiber absorbed solvent and began to dissolve under the attack of strong base system (DMSO/KOH), which further fell off from the surface and the ‘core’ area was exposed as shown in Fig. 5d₂. As more DMSO/KOH got inside of the fibers, the end and surface gloves of fiber were etched first due to the higher contact area with liquid, this made the macrofiber increasingly split into long strip shape along its longitudinal direction (Fig. 5d₃). Furthermore, the smaller rod-like structure of fiber was able to be clearly observed (Fig. 5d₄) when the reaction time was up to 60 h. It was inferred that the degradation of smaller rod-like structure of fiber was further conducted until the single fiber formed. And then the single fiber started to

Fig. 4 SEM images of aramid macrofibers: **a** F1, **b** F2, **c** F3 and **d** F4



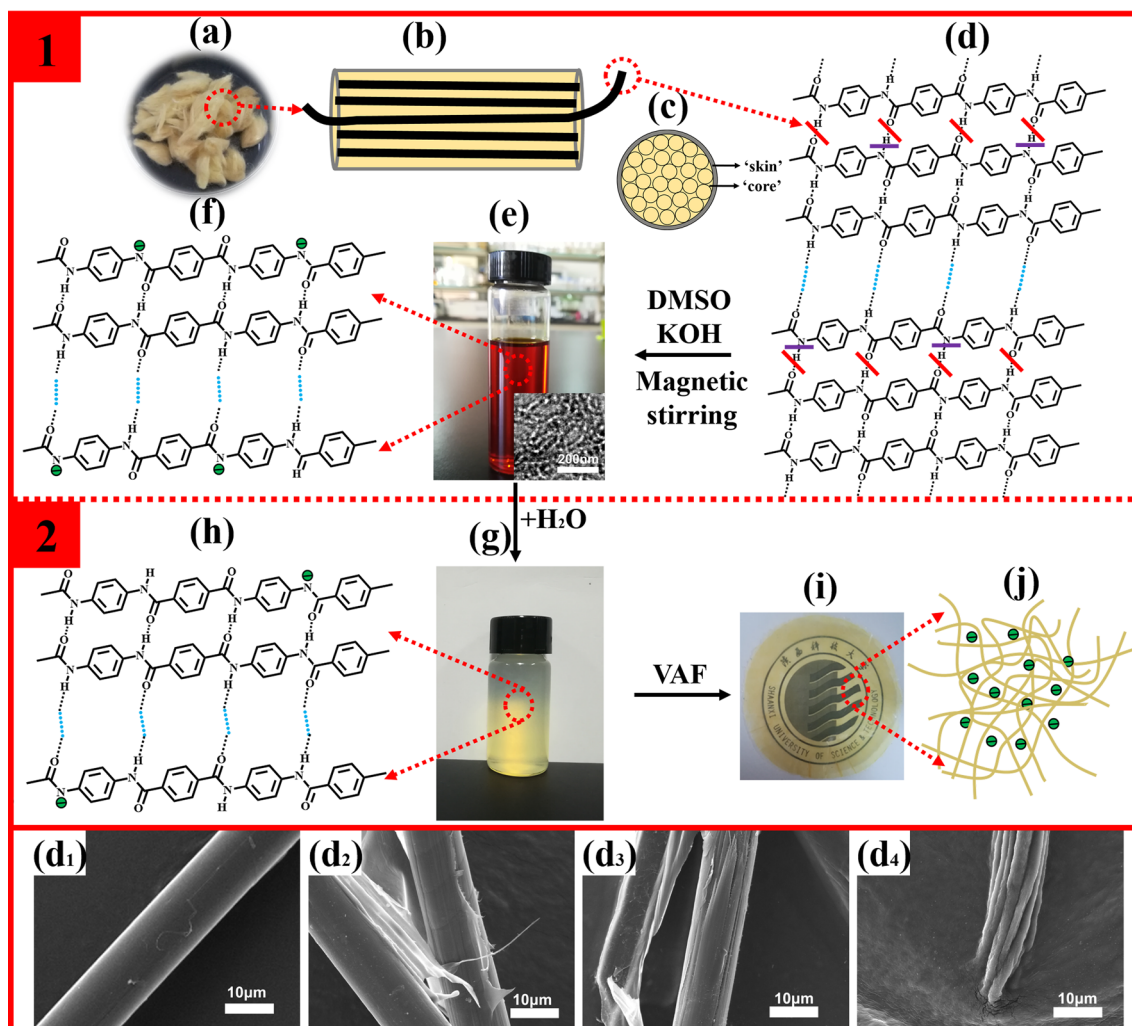


Fig. 5 1 The process of deprotonation of aramid macrofibers, d_1 – d_4 are SEM images of the chopped fiber in DMSO/KOH system for 0, 24, 36, 60 h, respectively; 2 partial protonation of ANFs and the formation of ANFs films

dissolve again similar to the process from Fig. 5d₃, d₄ until a homogeneous and transparent dispersion (Fig. 5e) containing uniformly dispersive nanofibers formed (the lower right corner in Fig. 5e). The process of macroscopical aramid fibers split into nanofibers as above is termed as deprotonation (Fig. 51).

The previous studies showed that the deprotonation of PPTA in DMSO/KOH system was directional and limited (Yang et al. 2011; Fan et al. 2012), which had greatly guaranteed the integrity of molecular chain of PPTA in length and was beneficial for the excellent mechanical performances for the final ANFs films. In addition, it has proved that the final nanofibers are negatively charged (the green cycle in Fig. 5f) with the broken N–H bonds (Guan et al. 2017). Therefore, here we believe that the deprotonation process of PPTA in the strong DMSO/KOH system involves two important parts, namely the destruction of intramolecular hydrogen bonds first (the red line in Fig. 5d) and then N–H

bonds from amide groups broken (the purple line in Fig. 5d). Therefore, the final dark red ANFs/DMSO dispersion stably generates under the balance of the electrostatic repulsion from the negatively charged nitrogen ions, π – π stacking in the polymer backbone and Van der Waals force between the polymer chains (Fan et al. 2012). Moreover, it is well known that the distance between the single molecular chain of molecular structure of PPTA is 0.3–0.5 nm (Rebouillat et al. 1999; Cao 2013), so the number of the rigid molecular chain (for chopped ANFs is between 41 and 72) can be estimated according to the diameter distribution offered by TEM images (Fig. 6j), which demonstrates that the explanation for the final aramid nanofibers composing of single molecular chain in some previous reports is probably problematic (Guan et al. 2017).

For the process of partial protonation (Fig. 52) process, two volumes of deionized water were added to obtain a ANFs/DMSO/H₂O mixture suspension (Fig. 5g), where the

Fig. 6 **a–d** SEM images of nanofibers from F1-ANFs to F4-ANFs; **e–h** TEM images of nanofibers from F1-ANFs to F4-ANFs; **i–l** statistical analysis of the diameter distribution of ANFs shown in **e–h**, respectively

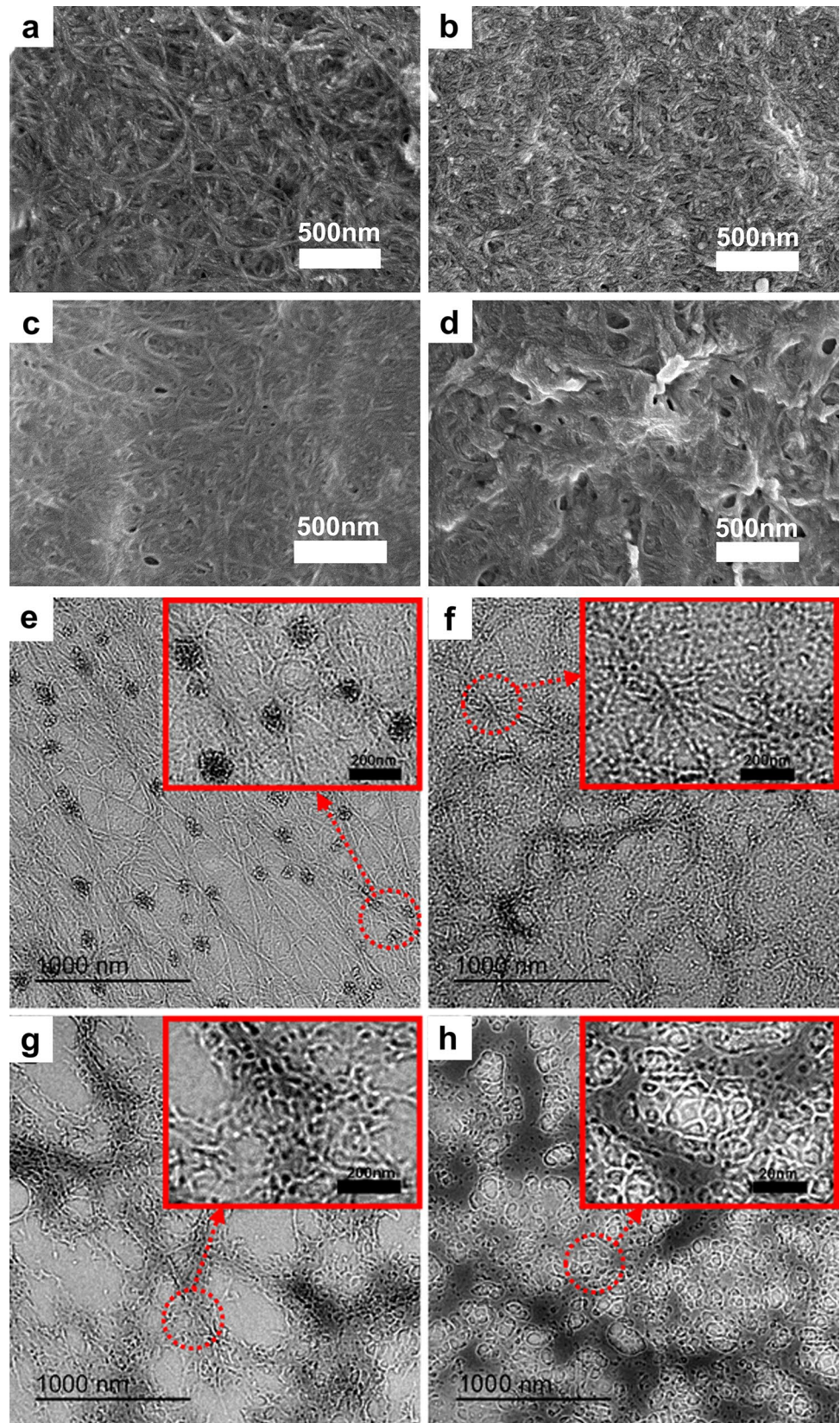
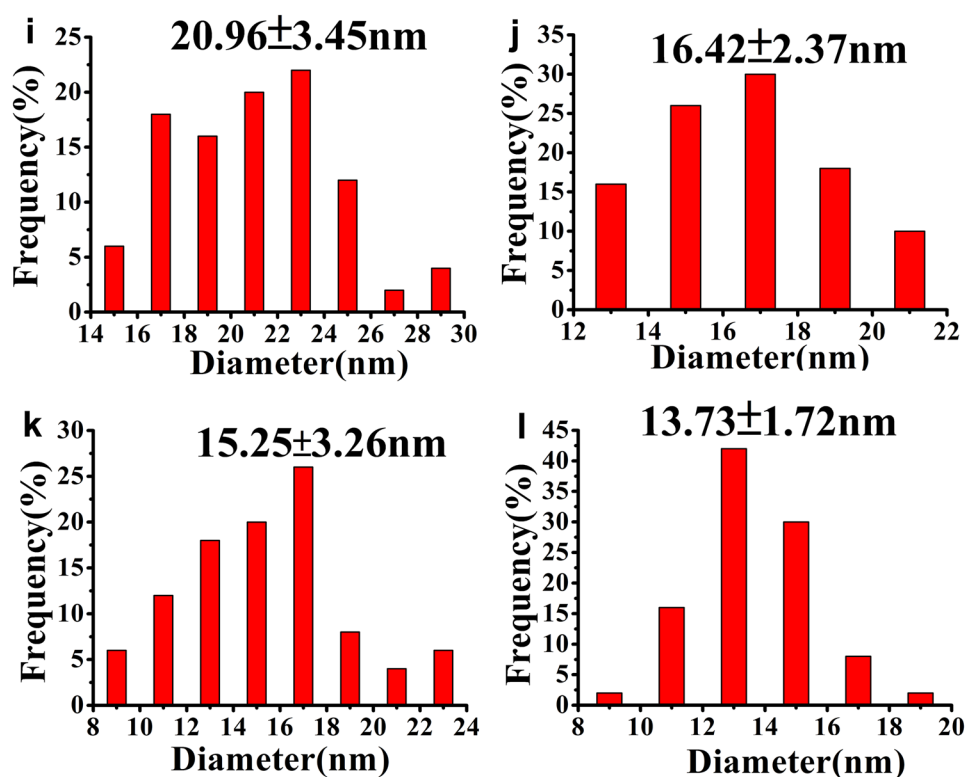


Fig. 6 (continued)



negatively charged nitrogen ions in ANFs were partly protonated as shown in Fig. 5h. Finally, the ANFs film (Fig. 5i) was collected using VAF and presented with certain transparency after the drying treatment, in which the partially protonated ANFs interconnected with each other (Fig. 5j) to generate certain strength.

The microscopic appearance and distribution of ANFs in DMSO

TEM and SEM images both were used to characterize the structure of the ANFs in DMSO. For SEM images (Fig. 6a–d), the dense spider-web-like network structure was observed in all the samples, which indicated that the nanoscale aramid fibers had been successfully prepared. Additionally, TEM images also offered the more detailed information of the formed ANFs (Fig. 6e–h), where many local weak points composing of a mass of lump fiber flocculation (Fig. 6e) were observed in yarns ANFs. However, the phenomenon for this was relatively rare in chopped ANFs (Fig. 6f) whilst nothing was able to be seen in ANFs of the pulp and fibril fibers (Fig. 6g, h).

The diameters of ANFs after the deprotonation of the different macroscopic aramid fibers lied in 12–25 nm as shown in Fig. 6i–l. From the material itself perspective, the changes can be attributed to the different penetration rate of solvent into the internal structure based on different the physical structures of raw materials. The length of F1-ANFs

(Fig. 6e) appeared to be in the range of 8–10 μm , F2-ANFs (Fig. 6f) reached to 4–6 μm , and F3-ANFs (Fig. 6g) was up to 2–3 μm . A special case (Fig. 6h) was that a great extent of twisting and winding happened in fibril ANFs, which made the length of the fiber not so clear. The difference of length distribution derived from the directional and limited deprotonation of PPTA along the fiber axis [28,30]. Therefore, the nanofibers of aramid yarns and chopped fibers with more obvious aspect ratio (the Table 1 in Sect. 2.1) than pulp fibers had longer length than that of pulp ANFs. For fibril ANFs, the unclear length information probably resulted from the soft and pleated ribbon-like film structure of the original structure of fibril fibers (Levit and Amma 2006; Kang et al. 2014).

Isolation of ANFs powder and observation of ANFs film

The previous studies have shown that the final ANFs/DMSO dispersion is very sensitive to humidity (Cao 2013). ANFs are quite easy to precipitate even if it is an ambient environment. It can be problematic that if the final nanofibers can only exist stably in the DMSO/KOH dispersion, which extremely restricts the application of ANFs for processing into high-performance nanocomposites. Therefore, it is essential to isolate and purify ANFs.

Naturally, any protonic donors such as DI water (Yang et al. 2011), alcohol and polyacrylic acid (PAA) (Yang et al.

2015) whose pKa value is higher than PPTA, can call be used to protonate ANFs (Burch and Manring 1991). However, the different proton donors bring completely different results especially mechanical properties to ANFs films. Ethanol is a weaker proton donor in comparison with DI water. Consequently, the ANFs-water (ANFs protonated by water) films interconnected with the nanoscaled pores have more excellent mechanical properties than the ANFs-ethanol films protonated by ethanol (Lyu et al. 2016a). High molecular organic acid PAA, whose pKa is even higher than water or ethanol (Yang et al. 2015), tends to interconnect with ANFs to prepare ANFs/PAA nanocomposite. In consideration of our intention is to explore the original properties of ANFs per se, it is necessary to decrease the complexity of the solution system. Meanwhile, the cost input and environmental pollution should also be taken into account against the actual conditions. Therefore, here DI water has been chosen as the cheapest and environmental proton donor to protonate ANFs.

Interestingly, a study has found that the solid ANFs prepared by adding equal volume of water to execute proton recovery, have the smaller diameter than the original ANFs in DMSO (Lin et al. 2017). Apparently, this provides additional opportunities for the isolated ANFs to be easier combined with other polymers due to the great abundance of polar functional groups onto it. Besides, the amount of proton donor also has a positive effect on the degree of protonation of ANFs (Yang et al. 2015). In our experiment, hence, twice volumes of deionized water than that of the ANFs/DMSO dispersion was added to achieve the protonation process. As a result, a uniformly mixed two-phase ANFs/water/DMSO suspension was obtained as seen in the Fig. 5g.

The solution processing techniques of film typically include layer-by-layer (LBL) (Kuang et al. 2015), spin-coating (Patil et al. 2003) and solvent casting (Park et al. 2006), tape-casting (El Hafiane et al. 2012) and VAF (Zhu et al. 2015). LBL and spin-coating are characterized by the preparation of ultrathin films with higher uniformity in comparison with the other techniques (Yang et al. 2011; Lyu et al. 2016a). However, the challenging problem in these methods lies in the fact that both of them are complicated and highly time-consuming in regulating the thickness of films. By contrast, the solvent casting and tape casting are easily achievable but have been severely limited by its low process controllability, which further leads to the poor uniformity of the film. As for VAF, the high efficiency of film production and good film homogeneity and uniformity make it an ideal method for the rapid production of high-quality membranes (Yang et al. 2015). Most noteworthy, ANFs films can be thought as one special paper sheet to some extent, whose preparation process of ANFs films is very similar to the traditional paper-making process mainly consisting of the fiber preparation,

dewatering and drying three parts (Yang et al. 2016). This makes the mass production or industrial development of ANFs films in the further become more possible and meaningful. Therefore, here VAF acting as the most simple and efficient phase separation technique is employed to quickly isolate the solid ANFs from the ANFs/water/DMSO system (Fan et al. 2012; Wang et al. 2013) to prepare ANFs films.

UV analysis

The transparency of the material is mainly determined by its transmittance in visible light and the degree of light scattering (Qian 2014). High transparency can be obtained when high transmittance and low light scattering are both achieved. Avoiding the mismatch of refractive indices between the fiber and the matrix can result in much less light scattering, and also the smaller size of nanofibers is conducive to obtain materials with higher transparency (Yang et al. 2015). Therefore, the pure ANFs films with smaller size both in length and diameter theoretically is available for the higher transparency. Our results (Fig. 7a) suggested that F4-ANFs showed the best property in transparency whose transmittance reached to 96%, whereas F1-ANFs was the worst one with the transmittance value of 73.4%, which were just within the expectation and could be explained by TEM information of differentiated distribution in length and diameter (Fig. 6i–l).

The degree of protonation of ANFs by adding deionized water was evaluated from UV–Vis absorbance spectra (Fig. 7b), where three visible absorption peaks were observed around 220, 280 and 405 nm, respectively. It is well known that the characteristic absorption peak of PPTA is at 250 and 330 nm, respectively, resulting from the π – π conjugated structure composing of amide group and the benzene ring in PPTA (Yu 2005). The absorption peak at 400 nm corresponds to the PPTA anions including the produced ANFs and the partially protonated ANFs (Yang et al. 2015). The obvious blue shift of characteristic absorption peak of PPTA can be attributed to the decreased electron cloud density and polarity of benzene ring in PPTA anions. The results verified that ANFs were just partially protonated when two equal volumes of deionized water were used to be as the proton donor, which is good for the stability and dispersion of ANFs/DMSO/H₂O system to further prepare transparent films of ANFs with good mechanical properties. Additionally, the intensity of absorbance peak of different ANFs films exhibited the opposite trend compared with transmittance spectra, except that some unexpected shifts occurred between F2-ANFs and F4-ANFs, which probably resulted from the poor smoothness of films.

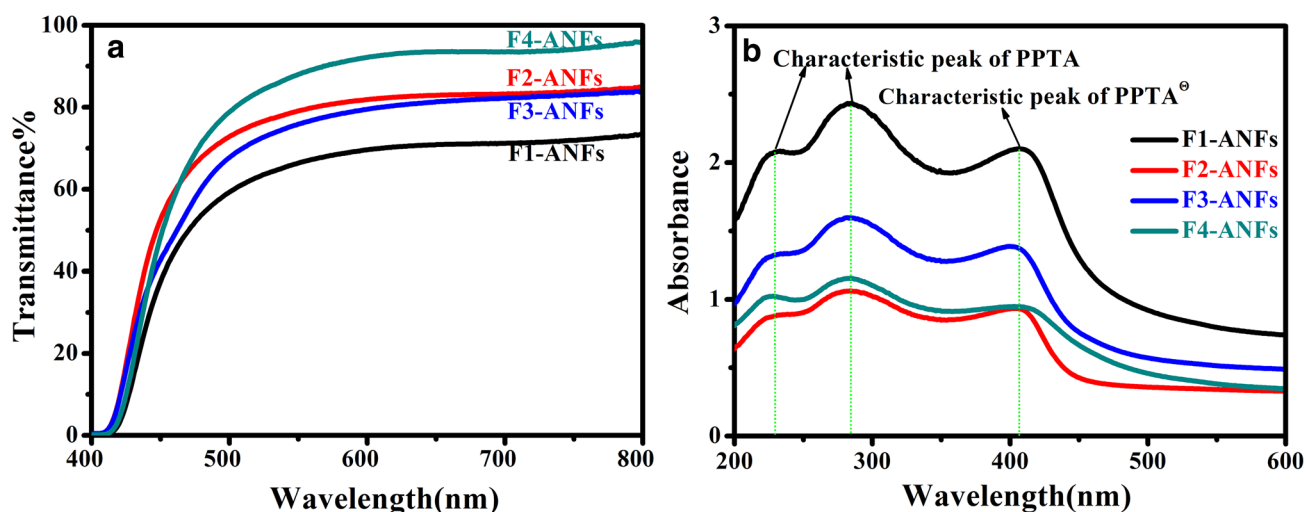


Fig. 7 UV-Vis spectra of pure ANFs films: **a** transmittance; **b** absorbance

FT-IR analysis

FT-IR spectra (Fig. 8a) was also conducted to compare the molecular structures of ANFs films with the original macrofibers. For the macroscopic fibers, the intensity and sharpness of IR peaks (especially N–H stretching vibrations) decreased from F1 to F4 due to the smaller association degree of hydrogen bond caused by mechanical cutting or the high degree of fibrillation treatment in the manufacturing process. In comparison with the macrofibers, the intensity and sharpness of IR peaks of ANFs films obviously reduced, which was attributed to the broader distribution of bond lengths and surface states of the fiber (Yang et al. 2011). Besides, the intensity and sharpness of IR peaks in yarns and chopped ANFs films decreased more obvious compared with the macrofibers than that in pulp and fibrillated ANFs films,

which probably caused by the higher degree of degradation in yarns and chopped fibers with high higher crystallinity. Moreover, it is worthy to note that the stretching vibration of N–H around 3300 cm^{-1} (Fig. 8b) was not clear while its blending vibration around 1539 cm^{-1} , deformation vibration at 1510 cm^{-1} (Fig. 8c) and out-plane blending vibration about 660 cm^{-1} (Fig. 8d) still existed. Although that both the deformation and out-plane blending vibrations of N–H moved to the lower wavenumbers compared with macrofibers due to the reduced electron cloud density and polarity of benzene ring in PPTA anions. All these proved that the deprotonation process of PPTA into ANFs happened by breaking the N–H bond of amide group, and also the protonation of ANFs by adding the two equal volumes of deionized water was also partially conducted, which matched well with the UV result (Fig. 7b).

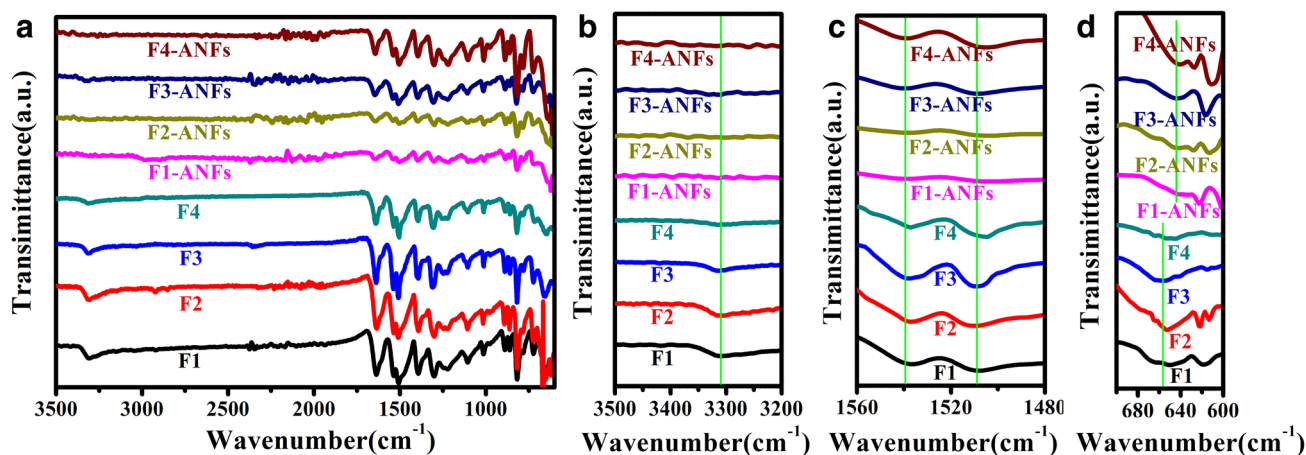


Fig. 8 IR spectra of macroscale aramid fibers and pure ANFs films: **a** the full spectra; **b** stretching vibration of N–H; **c** blending and deformation vibration of N–H and **d** out-plane blending vibration of N–H

XRD analysis

For the further study, XRD patterns were carried out to explore the crystallization property of macroscale (Fig. 9a) and nanoscale aramid fibers (Fig. 9b), where the crystallinity (Fig. 9c) was analysed by JADE5.0 software and the grain size was calculated basing on the Scherrer equation, $D=0.89\lambda/\beta\cos\theta$ (Yang et al. 2011). The characteristic PPTA peaks around $2\theta=20.6^\circ$, 22.8° and weak shoulder diffraction peak at 28.6° can be indexed as 100, 200 and 004 plane, respectively (Anjana and Vijayan 2000). However, the pattern was not suitable for all kinds of aramid macrofibers. Note that fibril fiber showed a clear difference from the samples whose 100 plane disappeared but another 002 plane with the diffraction angle $2\theta=15.2^\circ$ turned up. This suggested that fibril fibers had the lowest crystallinity compared with others as shown by cyan histogram in Fig. 9c, where the decreasing crystallizations was due to the different degrees of treatment of the raw materials. Figure 9b presented that the XRD pattern of nanoscale aramid fibers showed a quite difference compared with the original macrofibers, in which the 200 planes in all the ANFs samples could not be found. However, the 002 plane obviously appeared in all ANFs except from F1-ANFs. The crystallization of different ANFs (the dark blue line in Fig. 9c) indicated that the dissolution

and deprotonation of aramid macrofibers with DMSO/KOH had greatly destroyed the crystal structure of original fibers. In addition, grain sizes of ANFs (the red line in Fig. 9c) matched with the diameter distribution information offered by TEM images (Fig. 6i–l).

Mechanical properties of ANFs films

The typical stress strain curves, tensile strength, stiffness and strain at break for the pure ANFs films were illustrated in Fig. 10. It showed that the pure chopped ANFs film had the highest ultimate strength (σ) of 103.41 MPa whilst the fibril ANFs showed the smallest strength (σ) of 24.46 MPa (the cyan histogram in Fig. 10b). Nevertheless, the stiffness for the pure ANFs films (the red line in Fig. 10b) continuously increased from F1-ANFs (4.27 GPa) to F4-ANFs (10.49 GPa). Combining the diameter and length information offered by TEM images (Fig. 6i–l), it indicated that the larger size of nanofibers in length provided more interconnectivity for fibers to be interlaced with each other to form the dense and uniform spider-like web structure, which finally facilitated for gaining the higher ultimate strength. However, the oversized nanofiber in length would lead to the formation of flocculation (Fig. 6i) which further caused stress concentration and was adverse to form ANFs films

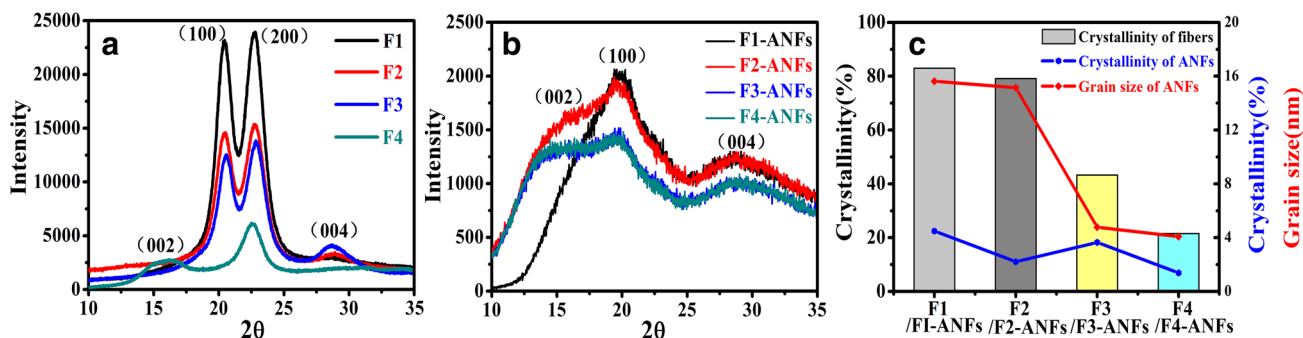


Fig. 9 XRD pattern: a macroscale aramid fibers, b pure ANFs films, c analysis of crystallization behavior

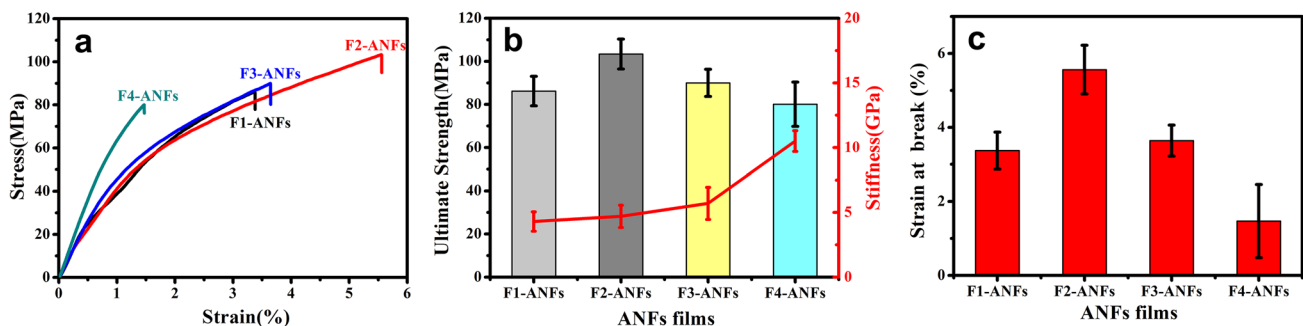


Fig. 10 Mechanical properties of pure ANFs films: a typical stress–strain curves, b ultimate strength and stiffness, c strain at break

with high strength. This can be used to explain the formation of the lower ultimate strength of yarns ANFs. Furthermore, the increased stiffness was contributed to the fact that the smaller diameter was conducive to form smaller pores being favorable for loading bearing and the achievement of higher stiffness. Besides, the strain at break of different ANFs films (Fig. 10c) showed that ANFs films with higher stiffness seemed to be more brittle. The chopped ANFs film kept the best flexibility or ductility whilst bearing the highest load, while the fibril ANFs was the most brittle one with strain of 1.47%, which probably resulted from the excessive stiffness (Guan et al. 2017). By contrast, F2-ANFs films exhibited better comprehensive mechanical properties with ultimate strength (σ) of 103.41 MPa, stiffness (E) of 4.70 GPa and strain at break of 5.56%.

Table 2 was further used to compare the performance differences of pure ANFs films in this work with that from the latest literatures. Surprisingly, our work first mentioned the ANFs films prepared by another kind of aramid macrofiber Twaron. It showed that the ANFs films prepared by Twaron fibers in this work had the comparable strength but relatively lower stiffness and strain at break than that made by Kevlar when the same film forming method VAF was employed, which probably attributed to the fact that the original Kevlar fiber manufactured by USA Dupont is superior to the Twaron made by Japan Teiji (Zhang 2009). Besides, it was easy to find that although the ANFs films prepared by LBL and spin-coating had relatively better mechanical properties than that made of VAF owing to the higher film uniformity they created as we discussed in Sect. 3.4. It is worth mentioning that VAF has been still frequently utilized for the ANFs film formation due to its simplicity and utility as mentioned earlier.

Thermogravimetric analysis

The thermal stability of aramid macrofibers and ANFs films were also investigated by TGA tests. As shown in Fig. 11a, the similar thermogravimetric behavior can be observed in all the samples which is generally divided into three stages, namely slow degradation, fast decomposition and carbon stabilization. At the beginning of the first stage of slow degradation, it can be found that a small weight loss happened before 100 °C primarily owing to the evaporation of residual moisture absorbed in original fibers and ANFs films (Guan et al. 2017). Obviously, the weight of ANFs dropped was faster than the original fibers due to the reduced crystallinity of ANFs as characterized by XRD (Fig. 9c). In the second stage of fast decomposition, the weight was nearly linear downward because of the breakage and degradation of PPTA macromolecule chains. Here, the thermal stability of ANFs was evaluated by the $TG_{10\%}$ (temperature of weight loss at 10%) (Fig. 11b). Besides, Tonset was used as the decomposition temperature of ANFs films, which was defined as the temperature of intersection from the baseline of stage of slow degradation and maximum slope of the fast decomposition (Stathokostopoulou and Tarantili 2014) as shown in Fig. 11c. There was an obvious shift that both the $TG_{10\%}$ and Tonset points moved toward the lower temperature from the raw materials to ANFs films, which were mainly contributed to the different treatments of raw materials and reduced crystallinity of ANFs films. By comparison with the other ANFs, chopped and pulp ANFs showed the better thermal stability with $TG_{10\%}$ around 521 °C. For the last stage of carbon stabilization, there was no obvious difference in the residual of the final aramid nanofibers.

Table 2 Performance comparison of the pure ANFs films

| Raw material | Forming method | Thickness (μm) | Stiffness (Gpa) | The ultimate strength (MPa) | Strain at break (%) | Literature |
|---------------------|----------------|-----------------------------|----------------------------------------|----------------------------------------|-----------------------------------------|--------------------|
| Kevlar 69 | LBL | 0.019 | 9 ± 1 | Not reported | Not reported | Yang et al. (2011) |
| Kevlar yarns | LBL | 2 | 12.7 ± 0.8 | 179.6 ± 6.2 | 1.875 | Zhu et al. (2015) |
| Kevlar 69 | Spin-coating | 5.5 | 4.5 (ANFs-water) 5.1 (ANFs-ethanol) | 182 (ANFs-water) 140 (ANFs-ethanol) | 10.5 (ANFs-water) 5.7 (ANFs-ethanol) | Lyu et al. (2016a) |
| Kevlar 69 | Spin-coating | 7.5 | 1.7 | 196 | 16.8 | Lyu et al. (2016b) |
| Kevlar [®] | VAF | 4–5 | 7.1 ± 0.3 | 153 ± 15 | 8 | Yang et al. (2015) |
| Kevlar [®] | VAF | Not reported | 6.27 | 79.1 | Not reported | Fan et al. (2013) |
| Kevlar 69 yarns | VAF | 13 ± 0.7 | 7.1 ± 0.3 | 53 ± 2 | 9 | Cao et al. (2013) |
| Kevlar 69 | VAF | 10–20 | 5.2 | 90 | 2.2 | Kwon et al. (2017) |
| Twaron yarns | VAF | 20 | 4.3 ± 0.75 | 86.19 ± 6.83 | 3.37 ± 0.5 | This article |
| Twaron chopped | VAF | 24 | 4.7 ± 0.86 | 103.4 ± 6.93 | 5.56 ± 0.66 | This article |
| Twaron pulp | VAF | 24 | 5.7 ± 1.24 | 90 ± 6.33 | 3.64 ± 0.42 | This article |
| Twaron fibril | VAF | 18 | 10.5 ± 0.8 | 80.1 ± 10.28 | 1.47 ± 0.99 | This article |

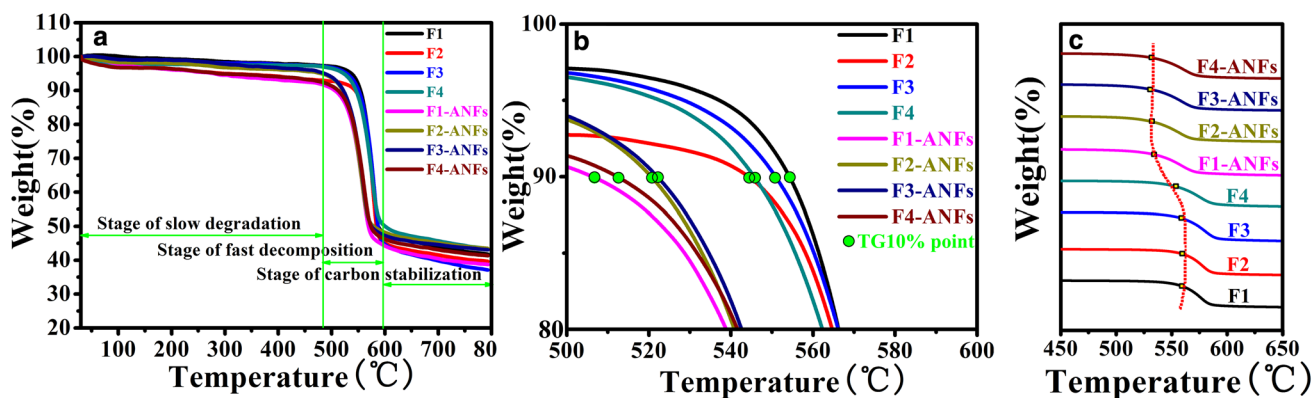


Fig. 11 Thermal stability of aramid macrofibers and pure ANFs films: **a** TGA curve, **b** the distribution of TG_{10%} points and **c** the distribution of Tonset points

Conclusion

In summary, ANFs with different diameters ranging from 12 to 25 nm were fabricated by effective deprotonation with KOH in DMSO from different forms of macroscale aramid fibers. Both of the ANFs powder and differentiated ANFs film were obtained via partial protonation of ANFs/DMSO dispersion with deionized water followed by simple VAF. We believe that the different morphologies and properties of aramid macrofibers promoted the formation of ANFs with differentiated lengths and diameters. Although the XRD result showed that the crystal structure of aramid macrofibers was greatly destroyed in the deprotonation process and low crystallinity of ANFs films was obtained, the final thermodynamic properties of ANFs films supported by TGA and tensile test evidences did not seem to be really influenced. The partial protonation of ANFs/DMSO dispersion was confirmed by UV absorbance and FI-TR characterization of ANFs films, whose optical performance was further confirmed by UV transmittance. By contrast, the ANFs films made from chopped nanofiber, whose aspect ratio was in the range of 200–500, exhibited good transparency, thermal stability and mechanical properties with transmittance value of 83%, TG_{10%} around 521 °C, ultimate strength (σ) of 103.41 MPa, stiffness (E) of 4.70 GPa and strain at break of 5.56%. We firmly believe that the result can provide an alternative nanoscale building block for preparing high-performance nanocomposites with different requirements in the area of transparent coating, flexible electrode or display material and battery separator.

Acknowledgements The authors sincerely appreciated the financial support from the National Key Research and Development Program (2017YFB0308300) and State Key Laboratory for Modification of Chemical Fibers and Polymers Materials (LK1601).

References

- Abdel-Bary EM, El-Nesr EM, Helaly FM (1997) Effect of gamma radiation-grafted aramid chopped fibers as the reinforcing filler in styrene-butadiene rubber mixtures. *Polym Adv Technol* 8:140–145. [https://doi.org/10.1002/\(sici\)1099-1581\(199703\)8:3<140:aid-pat642>3.0.co;2-u](https://doi.org/10.1002/(sici)1099-1581(199703)8:3<140:aid-pat642>3.0.co;2-u)
- Abu Obaid A, Deitzel JM, Gillespie JW, Zheng JQ (2011) The effects of environmental conditioning on tensile properties of high performance aramid fibers at near-ambient temperatures. *J Compos Mater* 45:1217–123. <https://doi.org/10.1177/0021998310381436>
- Anjana J, Vijayan K (2000) Kevlar 49 fibres: thermal expansion coefficients from high temperature X-ray data. *Currentence* 78(3):331–344
- Aranganathan N, Mahale V, Bijwe J (2016) Effects of aramid fiber concentration on the friction and wear characteristics of non-asbestos organic friction composites using standardized braking tests. *Wear* 354–355:69–77. <https://doi.org/10.1016/j.wear.2016.03.002>
- Barkoula NM, Alcock B, Cabrera NO, Peijs T (2008) Fatigue properties of highly oriented polypropylene tapes and all-polypropylene composites. *Polym Polym Compos* 16:101–113
- Burch RR, Manring LE (1991) *N*-alkylation and Hofmann elimination from thermal decomposition of R_4N^+ salts of aromatic polyamide polyanions: synthesis and stereochemistry of *N*-alkylated aromatic polyamides. *Macromolecules* 24(8):1731–1735
- Cao KQ (2013) Design and synthesis of reactive aramid nanostructures for advanced nanocomposites with tailored morphology and properties. Dissertation, University of Michigan
- Cao KQ, Siepermann CP, Yang M et al (2013) Reactive aramid nanostructures as high-performance polymeric building blocks for advanced composites. *Adv Funct Mater* 23(16):2072–2080. <https://doi.org/10.1002/adfm.201202466>
- El Hafiane Y, Smith A, Chartier T et al (2012) Role of dispersant and humidity on the setting of millimetric films of aluminous cement prepared by tape casting. *J Eur Ceram Soc* 32:2103–2111. <https://doi.org/10.1016/j.jeurceramsoc.2012.02.010>
- Fan JC, Shi ZX, Zhang L et al (2012) Aramid nanofiber-functionalized graphene nanosheets for polymer reinforcement. *Nanoscale* 4:7046. <https://doi.org/10.1039/c2nr31907a>
- Fan JC, Shi ZX, Tian M et al (2013) Graphene–aramid nanofiber nanocomposite paper with high mechanical and electrical performance. *RSC Adv* 3(39):17664–17667. <https://doi.org/10.1039/c3ra42515k>

- Faramarzi I, Razzaghi-Kashani M (2015) Improvements in tribological properties of polyamide 6 by application of aramid pulp. *Iran Polym J* 24:329–335. <https://doi.org/10.1007/s13726-015-0326-3> (English Edition)
- Gardner DJ, Oporto GS, Mills R, Samir MASA (2008) Adhesion and surface issues in cellulose and nanocellulose. *J Adhes Sci Technol* 22:545–567. <https://doi.org/10.1163/156856108x295509>
- Grujicic M, Yavari R, Ramaswami S et al (2013) Molecular-level study of the effect of prior axial compression/torsion on the axial-tensile strength of PPTA fibers. *J Mater Eng Perform* 22:3269–3287. <https://doi.org/10.1007/s11665-013-0648-2>
- Guan Y, Li W, Zhang YL et al (2017) Aramid nanofibers and poly (vinyl alcohol) nanocomposites for ideal combination of strength and toughness via hydrogen bonding interactions. *Compos Sci Technol* 144:193–201. <https://doi.org/10.1016/j.compscitech.2017.03.010>
- Hendriks AJJ, Wilbers D, Grotendorst H, et al (2004) *Para*-aramid fibril film. Patent, US9194061B2
- Kang BS, Levit MR, Marek RP et al (2014) Development of a new solid insulation for liquid-immersed transformers. *Electr Insul Conf* 2014:344–347
- Kapoor R, Pangeni L, Bandaru AK et al (2016) High strain rate compression response of woven Kevlar reinforced polypropylene composites. *Compos B Eng* 89:374–382. <https://doi.org/10.1016/j.compositesb.2015.11.044>
- Kim SJ, Cho MH, Lim D-S, Jang H (2001) Synergistic effects of aramid pulp and potassium titanate whiskers in the automotive friction material. *Wear* 251:1484–1491. [https://doi.org/10.1016/S0043-1648\(01\)00802-x](https://doi.org/10.1016/S0043-1648(01)00802-x)
- Kuang QX, Zhang D, Yu JC et al (2015) Toward record-high stiffness in polyurethane nanocomposites using aramid nanofibers. *J Phys Chem C* 119:27467–27477. <https://doi.org/10.1021/acs.jpcc.5b08856>
- Kwon SR, Harris J, Zhou TY et al (2017) Mechanically strong graphene/aramid nanofiber composite electrodes for structural energy and power. *ACS Nano* 11(7):6682–6690. <https://doi.org/10.1021/acsnano.7b00790>
- Lee JU, Park B, Kim BS et al (2016) Electrophoretic deposition of aramid nanofibers on carbon fibers for highly enhanced interfacial adhesion at low content. *Compos A Appl Sci Manuf* 84:482–489. <https://doi.org/10.1016/j.compositesa.2016.02.029>
- Levit MR, Amma A (2006) *Para*-aramid pulp including meta-aramid fibrils and processes of making same. Patent, EP1974093B1
- Li JB, Fan JC, Liao KX et al (2016) Facile fabrication of a multi-functional aramid nanofiber-based composite paper. *RSC Adv* 6:90263–90272. <https://doi.org/10.1039/c6ra15895a>
- Lin JJ, Bang SH, Malakooti MH, Sodano HA (2017) Isolation of aramid nanofibers for high strength and toughness polymer nanocomposites. *ACS Appl Mater Interfaces* 9:11167–11175. <https://doi.org/10.1021/acsmater.7b01488>
- Lu ZQ, Jiang M, Zhang MY, Xia XX (2016) Characteristics of PPTA chipped fiber/fibril and their properties for sheet making. *J Eng Fibers Fabr* 11:1–8
- Lu ZQ, Hu WJ, Xie F, Hao YS (2017) Highly improved mechanical strength of aramid paper composite via a bridge of cellulose nanofiber. *Cellulose* 24:2827–2835. <https://doi.org/10.1007/s10570-017-1315-9>
- Lyu J, Liu LH, Zhao X et al (2016a) Facile fabrication of multi-functional aramid nanofiber films by spin coating. *J Mater Eng Perform* 25:4757–4763. <https://doi.org/10.1007/s11665-016-2350-7>
- Lyu J, Wang XZ, Liu LH et al (2016b) High strength conductive composites with plasmonic nanoparticles aligned on aramid nanofibers. *Adv Funct Mater* 26:8435–8445. <https://doi.org/10.1002/adfm.201603230>
- Mishra RR, Kumar ANV, Rajesha S (2014) High velocity impact analysis of Kevlar composite by MATLAB. *Indian J Adv Chem Sci* 2:68–71
- Nie CX, Yang Y, Peng ZH et al (2017) Aramid nanofiber as an emerging nanofibrous modifier to enhance ultrafiltration and biological performances of polymeric membranes. *J Membr Sci* 528:251–263. <https://doi.org/10.1016/j.memsci.2016.12.070>
- Nilakantan G, Merrill RL, Keefe M et al (2015) Experimental investigation of the role of frictional yarn pull-out and windowing on the probabilistic impact response of Kevlar fabrics. *Compos B Eng* 68:215–229. <https://doi.org/10.1016/j.compositesb.2014.08.033>
- O'Connor I, Hayden H, O'Connor S et al (2009) Polymer reinforcement with Kevlar-coated carbon nanotubes. *J Phys Chem C* 113:20184–20192. <https://doi.org/10.1021/jp9046566>
- Park JM, Kim DS, Kim SR (2003) Improvement of interfacial adhesion and nondestructive damage evaluation for plasma-treated PBO and Kevlar fibers/epoxy composites using micromechanical techniques and surface wettability. *J Colloid Interface Sci* 264:431–445. [https://doi.org/10.1016/S0021-9797\(03\)00419-3](https://doi.org/10.1016/S0021-9797(03)00419-3)
- Park J, Lee S, Lee HH (2006) High-mobility polymer thin-film transistors fabricated by solvent-assisted drop-casting. *Org Electron Phys Mater Appl* 7:256–260. <https://doi.org/10.1016/j.orgel.2006.03.008>
- Park B, Lee W, Lee E et al (2015) Highly tunable interfacial adhesion of glass fiber by hybrid multilayers of graphene oxide and aramid nanofiber. *ACS Appl Mater Interfaces* 7:3329–3334. <https://doi.org/10.1021/am5082364>
- Patil KR, Sathaye SD, Kholam YB et al (2003) Preparation of TiO₂ thin films by modified spin-coating method using an aqueous precursor. *Mater Lett* 57:1775–1780. [https://doi.org/10.1016/S0167-577x\(02\)01067-4](https://doi.org/10.1016/S0167-577x(02)01067-4)
- Qian HX (2014) Research on durability and transparency on superhydrophobic surface. Dissertation, North China Electric Power University
- Qin ML, Kong HJ, Zhang K et al (2017) Simple synthesis of hydroxyl and ethylene functionalized aromatic polyamides as sizing agents to improve adhesion properties of aramid fiber/vinyl epoxy composites. *Polymers* 9:143. <https://doi.org/10.3390/polym9040143>
- Rebouillat S, Peng JCM, Donnet J-B (1999) Surface structure of Kevlar® fiber studied by atomic force microscopy and inverse gas chromatography. *Polymer* 40:7341–7350. [https://doi.org/10.1016/S0032-3861\(99\)00040-3](https://doi.org/10.1016/S0032-3861(99)00040-3)
- Ren J, Xu SQ, Liu QX et al (2014) Properties and applications of fibril. *China Text Lead* 10:68-7
- Sa R, Yan Y, Wei ZH et al (2014) Surface modification of aramid fibers by bio-inspired poly(dopamine) and epoxy functionalized silane grafting. *ACS Appl Mater Interfaces* 6:21730–21738. <https://doi.org/10.1021/am507087p>
- Salehi-Khojin A, Stone JJ, Zhong W-H (2007) Improvement of interfacial adhesion between UHMWPE fiber and epoxy matrix using functionalized graphitic nanofibers. *J Compos Mater* 41:1163–1176. <https://doi.org/10.1177/0021998306067301>
- Schmitt M, Ortlepp G (2008) Method for producing fibril-exhibiting high-performance chopped fibers, fibril-exhibiting high-performance chopped fibers, and articles containing the same. Patent, US20100206684A1
- Srinivasan G, Reneker DH (1995) Structure and morphology of small-diameter electrospun aramid fibers. *Polym Int* 36:195–201. <https://doi.org/10.1002/pi.1995.210360210>
- Stathokostopoulou C, Tarantili PA (2014) Preparation, characterization and drug release studies from poly(D, L-lactac acid)/organoclay nanocomposite films. *J Macromol Sci Part A* 51:117–124. <https://doi.org/10.1080/10601325.2014.864920>
- Takayanagi M, Kajiyama T, Katayose T (1982) Surface-modified Kevlar fiber-reinforced polyethylene and ionomer. *J Appl Polym Sci* 27:3903–3917. <https://doi.org/10.1002/app.1982.070271024>

- Thomas D (2017) Developing enhanced carbon nanotube reinforced composites for full-scale 3D printed components. *Reinf Plast*. <https://doi.org/10.1016/j.repl.2017.06.089>
- Wang JZ, Lu L, Lotya M et al (2013) Development of MoS₂-CNT composite thin film from layered MoS₂ for lithium batteries. *Adv Energy Mater* 3:798–805. <https://doi.org/10.1002/aenm.201201000>
- Widodo M, El-Shafei A, Hauser PJ (2012) Surface nanostructuring of Kevlar fibers by atmospheric pressure plasma-induced graft polymerization for multifunctional protective clothing. *J Polym Sci Part B Polym Phys* 50:1165–1172. <https://doi.org/10.1002/polb.23098>
- Wollbrett-Blitz J, Joannès S, Bruant R et al (2015) Multiaxial mechanical behavior of aramid fibers and identification of skin/core structure from single fiber transverse compression testing. *J Polym Sci Part B Polym Phys*. <https://doi.org/10.1002/polb.23763>
- Wright TM, Carr CM, Grant CA et al (2015) Strength of hydroentangled fabrics manufactured from photo-irradiated poly *para*-phenylene terephthalamide (PPTA) fibres. *Polym Degrad Stab* 121:193–199. <https://doi.org/10.1016/j.polymdegradstab.2015.08.017>
- Wu SG, Yaru F, Zhou J (2012) Research progress on preparation methods of PMIA fiber. *Adv Mater Res* 11, Pts 1 and 2 463–464:769–772. doi: 10.4028/www.scientific.net/AMR.463-464.769
- Yang M, Cao KQ, Sui L et al (2011) Dispersions of aramid nanofibers: a new nanoscale building block. *ACS Nano* 5:6945–6954. <https://doi.org/10.1021/nn2014003>
- Yang M, Cao QK, Yeom B et al (2015) Aramid nanofiber-reinforced transparent nanocomposites. *J Compos Mater* 49:1873–1879. <https://doi.org/10.1177/0021998315579230>
- Yang B, Lu ZQ, Zhang MY et al (2016) A ductile and highly fibrillating PPTA-pulp and its reinforcement and filling effects of PPTA-pulp on properties of paper-based materials. *J Appl Polym Sci* 133:1–6. <https://doi.org/10.1002/app.43209>
- Yu B (2005) Progress in production and application of *p*-aramid fibers (π). *Synth Technol Appl* 20(3):22–28
- Zhang YH (2009) Influence of γ -ray irradiation modification on properties of aramid fiber and its composites. Dissertation, Harbin Institute of Technology
- Zhu J, Cao W, Yue M et al (2015) Strong and stiff aramid nanofiber/carbon nanotube nanocomposites. *ACS Nano* 9:2489–2501

Publisher's Note Springer Nature remains neutral with regard to jurisdictional claims in published maps and institutional affiliations.